Available online at www.sciencedirect.com
ScienceDirect
Acta Materialia 59 (2011) 1761–1771
Acta MATERIALIA
www.elsevier.com/locate/actamat

Crystal plasticity finite-element analysis versus experimental results of pyramidal indentation into (0 0 1) fcc single crystal

Bernhard Eidel *

Interdisciplinary Centre for Advanced Materials Simulation (ICAMS), Ruhr-Universität Bochum, Stiepeler Strasse 129, D-44801 Bochum, Germany

Received 19 October 2010; accepted 17 November 2010
Available online 28 December 2010

Abstract

Pyramidal microindentation into the (0 0 1) surface of an face-centered cubic (fcc) single crystal made of a Ni-base superalloy is analyzed in experiment and crystal plasticity finite-element simulations. The resultant material pile-up at the surface reflects the material's symmetry and turns out to be insensitive to different loading scenarios as induced by (i) different azimuthal orientations of the pyramidal indenter, (ii) different indenter shapes (sphere or pyramid) and (iii) the elastic anisotropy. Experiments and simulations are in agreement and suggest that pile-up deformation patterns merely depend on the geometry of discrete slip systems but are invariant to different anisotropic stress distributions as induced by (i)–(iii). The local adaption of pile-up to the pyramidal indenter leads to convex or concave indent shapes corresponding to the indenter orientation. We contrast the present findings for curved indent shapes of fcc single crystals to similar, well-known observations for quasi-isotropic polycrystals. Although phenomenologically similar in kind, the driving mechanisms are different: for the single crystal it is the discrete and anisotropic nature of plastic glide in certain slip systems; for isotropic polycrystals it is the rate of strain-hardening caused by the cumulative response of dislocations.

Keywords: Crystal plasticity; Micromechanical modeling; Indentation; Anisotropy; Ni alloys

1. Introduction

Indentation into single-crystalline material has attracted interest in the experimental, modeling and computational branches of materials science for several reasons. One reason is that the simple, homogeneous microstructural composition enables identification of elementary deformation mechanisms without the complexity of heterogeneous, polycrystalline or multiphase systems. An important aspect of such indentation experiments is the possibility to draw inferences from surface deformation phenomena, such as pile-up or sink-in, to material properties and processes in the bulk of the material. Early studies used etch-pitting to measure densities of dislocations in the bulk of the material. This information, along with slip-line studies at indented surfaces, provides information on active slip systems (e.g. [1]). Based on this type of slip-line analysis, novel techniques have been developed to identify the orientation of an fcc single crystal (cf. [2]).

The study of single crystals in indentation has been boosted by the development of advanced methods of microscopy along with image processing and visualization. Details of surface topographies have been studied with high fidelity down to the nanoscale. Scanning tunneling microscopy (STM) has been used [3] to discuss mechanisms of plastic flow based on pile-up pattern around Vickers indents and to study the indentation size effect (ISE) for micron-sized body-centered cubic (bcc) single crystals. Atomic force and orientation imaging microscopy has been applied to analyze slip step formation around indents and hence to provide information on active slip systems and dislocation reactions [4]. Scanning electron microscopy (SEM) was applied to investigate anisotropic surface

* Present address: Institut für Mechanik, Universität Duisburg-Essen, Universitätsstrasse 15, D-45141 Essen, Germany. Tel.: +49 201 183 2708; fax: +49 201 183 2680.
E-mail address: bernhard.eidel@uni-due.de
URL: http://www.uni-due.de/mechanika/.

1359-6454/$36.00 © 2010 Acta Materialia Inc. Published by Elsevier Ltd. All rights reserved.
doi:10.1016/j.actamat.2010.11.042

topographies in (0 0 1), (1 1 0) and (1 1 1) oriented NiAl via spherical indentation [5]. For the same set of orientations, pile-up patterns were analyzed for nanoindentation into fcc single-crystalline copper by means of both electron backscatter diffraction (EBSD) techniques and simulation [6]. Rotation patterns below nanoindents were measured by EBSD tomography in Ref. [7].

In order to avoid symmetries different from those of the crystal, spherical or conical indenters have been used in the majority of cases to study pile-up in fcc single crystals [6–14]. For the same reason the use of sharp indenters for analyzing pile-up formation is rather rare [15–17], and simulations in this direction have had a focus rather on hardness, force–depth curves for prestrained and annealed crystals [18,19], but not on surface topographies in particular.

The main thrust of the present work is to investigate explicitly the complementary case, where the indenter is not isotropic and where the indenter's symmetries do not necessarily coincide with those of the crystal. With that aim, a pyramidal indenter is used for indentation into (0 0 1) fcc single crystal in order to answer the following questions:

(i) How does an indenter's pyramidal shape, which is accompanied by corresponding stress concentrations, influence the elastoplastic pile-up deformations of an fcc single crystal? How does the variation of the indenter's azimuthal orientation influence the results?
(ii) Can the asymmetry imposed by a pyramidal indenter break the material symmetries of the crystal leading to pile-up pattern different from geometrically isotropic spherical indentation?

Apart from the indenter's geometry, it is in the first place the elastic anisotropy which governs the stress response of the material. For strong anisotropy in the elasticity law, measured in terms of the Zener anisotropy ratio $AR = 2c_{44}/(c_{11} - c_{12})$, the material subject to (indentation) strain will attract stress in the directions of higher stiffness. Hence, it is a completion of the above questions to ask:

(iii) Is the indentation pattern invariant with respect to variations of stress as induced by different elasticity laws?

In order to answer question (iii) we single out the influence of the anisotropy in the elasticity law simply by applying isotropic elasticity while maintaining the anisotropy of plastic slip in the crystal plasticity model.

In summary, measurements (i)–(iii) systematically vary the stress distribution in the indented single crystal while the orientation of the crystal's slip systems is kept fixed. Hence, the simulation and experimental study of this work aims to analyze the importance of mechanical stress in fcc single crystals for pile-up formation during indentation.

With these aims in mind, the paper is structured as follows. To put things into perspective we summarize in Section 2 the basics of the crystal plasticity model used in the finite-element analysis. Next, we address aspects of modeling the two-phase Ni-base superalloy concerning its composition and hardening behavior. Section 3 describes the post-processing of the indentation experiment along with experimental techniques to obtain a 3-D picture of the indentation topographies. In Section 4 we present the crystal plasticity finite-element analysis of pyramidal–and for comparison spherical–indentation into the (0 0 1) fcc single crystal for various indenter orientations. Simulation and experiment are compared in Section 5. Based on these data we conclude in Section 6 on the driving mechanism behind the surface deformation patterns and its sensitivity with respect to indenter orientation, indenter shape and to the anisotropy of the elasticity law. Since quasi-isotropic polycrystals have shown similar indent shapes as the (0 0 1) fcc single crystal, we conclude the present analysis by contrasting the two, different driving mechanisms, which lead to strikingly similar phenomena.

2. The constitutive model

We will first consider the kinematics and constitutive equations of the single-crystal plasticity model used in the simulations. Next, we address aspects of modeling the present single-crystalline material, a Ni-base two-phase superalloy, concerning its composition and hardening behavior.

The foundations of single-crystal plasticity may be traced back to Refs. [20–26]. The computations presented are performed with the finite-element program Abaqus [27] with a user-material subroutine UMAT for single-crystal plasticity written by Ref. [28] as modified in Ref. [29]. The formulation in the UMAT follows the theoretical framework in Refs. [25,30].

2.1. Kinematics and the crystal plasticity model

We consider a crystalline body $\Omega \subset \mathbb{R}^3$ undergoing an elastoplastic deformation $\varphi : \Omega \to \mathbb{R}^3$ with a deformation gradient $\mathbf{F} = \partial_{\mathbf{X}}\varphi(\mathbf{X})$ and a Jacobian $J = \det\mathbf{F} > 0$, where $\mathbf{X}$ designates a material point in the reference configuration.

The multiplicative decomposition of the total deformation gradient

$$\mathbf{F} = \mathbf{F}^e\mathbf{F}^p, \tag{1}$$

as proposed in Ref. [31,32] is assumed to hold. $\mathbf{F}^p$ represents plastic simple shears that do not change the lattice geometry, $\mathbf{F}^e$ represents stretching and rotation of the lattice. The decomposition in Eq. (1) along with the definition of the velocity gradient $\mathbf{L} = \dot{\mathbf{F}}\mathbf{F}^{-1}$ implies an additive decomposition of $\mathbf{L}$ in the format:

$$\mathbf{L} = \mathbf{L}^e + \mathbf{F}^e\mathbf{L}^p\mathbf{F}^{e-1}, \tag{2}$$

with $\mathbf{L}^e = \dot{\mathbf{F}}^e\mathbf{F}^{e-1}$, $\mathbf{L}^p = \dot{\mathbf{F}}^p\mathbf{F}^{p-1}$ the elastic and plastic distortion rates, respectively. A superposed dot refers to a material time derivative. The elastic and inelastic stretching and spin tensors are defined as:

$$\begin{aligned}\mathbf{D}^e &= \operatorname{sym}\mathbf{L}^e, \quad \mathbf{W}^e = \operatorname{skw}\mathbf{L}^e,\\ \mathbf{D}^p &= \operatorname{sym}\mathbf{L}^p, \quad \mathbf{W}^p = \operatorname{skw}\mathbf{L}^p,\end{aligned} \tag{3}$$

such that the decompositions $\mathbf{L}^e = \mathbf{D}^e + \mathbf{W}^e$ and $\mathbf{L}^p = \mathbf{D}^p + \mathbf{W}^p$ hold.

It is assumed that plastic flow is mediated by the movement of dislocations on well-defined slip systems $\alpha = 1,2,\ldots,N$ in the crystal lattice with the slip direction $\mathbf{s}_0^\alpha$ and slip plane normal $\mathbf{n}_0^\alpha$ in the αth slip system, where $\mathbf{s}_0^\alpha \cdot \mathbf{n}_0^\alpha = 0$, $|\mathbf{s}_0^\alpha| = |\mathbf{n}_0^\alpha| = 1$, $\mathbf{s}_0^\alpha,\ \mathbf{n}_0^\alpha = \text{constant}$. For fcc single crystals there are $N = 12$ octahedral slip systems, referred to as $(1\,1\,1)\ \langle 1\,1\,0\rangle$ slip systems.

Introducing the Schmid tensor with symbol $\otimes$ as the dyadic product of two vectors:

$$\mathbb{S}_0^\alpha = \mathbf{s}_0^\alpha \otimes \mathbf{n}_0^\alpha, \tag{4}$$

the plastic distortion rate which sums up the shearing rates on all slip systems can be written as:

$$\mathbf{L}^p = \dot{\mathbf{F}}^p\mathbf{F}^{p-1} = \sum_{\alpha=1}^{N} \dot\gamma^\alpha \mathbb{S}_0^\alpha, \tag{5}$$

where $\dot\gamma^\alpha$ is the plastic shear strain rate in the αth slip system. Hence, the plastic stretching $\mathbf{D}^p$ and the plastic spin $\mathbf{W}^p$ can be represented as:

$$\begin{aligned}\mathbf{D}^p &= \sum_{\alpha=1}^{N} \dot\gamma^\alpha \mathbf{P}^\alpha, \quad \text{with } \mathbf{P}^\alpha = \operatorname{sym}\mathbb{S}_0^\alpha,\\ \mathbf{W}^p &= \sum_{\alpha=1}^{N} \dot\gamma^\alpha \mathbf{W}^\alpha, \quad \text{with } \mathbf{W}^\alpha = \operatorname{skw}\mathbb{S}_0^\alpha.\end{aligned} \tag{6}$$

The Cauchy stress tensor $\boldsymbol{\sigma}$ induces the resolved shear stress τ^α on the αth slip system according to:

$$\tau^\alpha = \mathbb{S}_0^\alpha : \boldsymbol{\sigma}. \tag{7}$$

In the elastoviscoplastic approximation of the rate-independent model, the shearing rate $\dot\gamma^\alpha$ can be expressed as a rate-dependent power-law [26]:

$$\dot\gamma^\alpha = \dot\gamma_0 \left|\frac{\tau^\alpha}{\tau_r^\alpha}\right|^{1/m} \operatorname{sgn}(\tau^\alpha), \tag{8}$$

where $1/m$ is the rate sensitivity exponent, $\dot\gamma_0$ is the shear strain rate at a reference condition and τ_r^α denotes the current shear strength of the αth slip system. The rate-independent limit is achieved for $m \to 0$. τ_r^α develops with the evolution of slips on active slip systems due to the accumulation of dislocations in a crystal, i.e. work-hardening. Since work-hardening of slip systems depends on inelastic shear deformations, the rate of τ_r^α is calculated by:

$$\dot\tau_r^\alpha = \sum_{\beta=1}^{N} h^{\alpha\beta}|\dot\gamma^\beta|, \tag{9}$$

where matrix $[h^{\alpha\beta}]$ describes the increase of the deformation resistance on slip system α due to shearing on system β. The diagonal components ($\alpha = \beta$) describe self-hardening, the off-diagonal components ($\alpha \neq \beta$) represent latent-hardening.

For hyperelasticity, the Cauchy stress $\boldsymbol{\sigma}$ is related to the elastic strain-rate $\mathbf{D}^e$ by:

$$\overset{\nabla}{\boldsymbol{\sigma}}{}^e = \mathbb{C}^e : \mathbf{D}^e - \boldsymbol{\sigma}\operatorname{tr}(\mathbf{D}^e) = \mathbb{C}^e : (\mathbf{D} - \mathbf{D}^p) - \boldsymbol{\sigma}\operatorname{tr}(\mathbf{D}), \tag{10}$$

see, for example, Ref. [33], where $\mathbb{C}^e$ is the tensor of elastic moduli with three independent elasticity constants, c_{11}, c_{12} and c_{44}, for crystals with cubic symmetries. The Jaumann rate $\overset{\nabla}{\boldsymbol{\sigma}}{}^e$ is the co-rotational stress rate in the coordinate system that spins with the lattice:

$$\overset{\nabla}{\boldsymbol{\sigma}}{}^e = \overset{\nabla}{\boldsymbol{\sigma}} + \mathbf{W}^p \cdot \boldsymbol{\sigma} - \boldsymbol{\sigma} \cdot \mathbf{W}^p, \tag{11}$$

where $\overset{\nabla}{\boldsymbol{\sigma}} = \dot{\boldsymbol{\sigma}} - \mathbf{W}\cdot\boldsymbol{\sigma} + \boldsymbol{\sigma}\cdot\mathbf{W}$ is the co-rotational stress rate on axes that spin with the material. Inserting Eqs. (10) and (6) into Eq. (11) and solving for $\overset{\nabla}{\boldsymbol{\sigma}}$ results in:

$$\overset{\nabla}{\boldsymbol{\sigma}} = \mathbb{C}^e : \mathbf{D} - \boldsymbol{\sigma}\operatorname{tr}(\mathbf{D}) - \sum_{\alpha=1}^{N} [(\mathbf{W}^\alpha \cdot \boldsymbol{\sigma} - \boldsymbol{\sigma}\cdot\mathbf{W}^\alpha + \mathbb{C}^e : \mathbf{P}^\alpha)]\dot\gamma^\alpha. \tag{12}$$

The elastoplastic deformation of the crystal manifests in lattice rotation and distortion, which results in slip directions and slip normals in the current configuration according to: $\mathbf{s}^\alpha = \mathbf{F}^e \cdot \mathbf{s}_0^\alpha$ and $\mathbf{m}^\alpha = \mathbf{m}_0^\alpha \cdot \mathbf{F}^{e-1}$.

Hence, they follow the evolution equations:

$$\dot{\mathbf{s}}^\alpha = \mathbf{L}^e \cdot \mathbf{s}_0^\alpha, \quad \dot{\mathbf{m}}^\alpha = -\mathbf{m}_0^\alpha \cdot \mathbf{L}^e. \tag{13}$$

Evolution Eqs. (9), (12) and (13) are cast into a time-discrete format for time integration.

2.2. Hardening law

The first model, which incorporates both linear isotropic hardening and self-hardening, was proposed in Ref. [34] (see also Ref. [25]). In this case, the hardening matrix $[h^{\alpha\beta}]$ in Eq. (9) is of the format:

$$h^{\alpha\beta} = h[q + (1-q)\delta^{\alpha\beta}]. \tag{14}$$

Herein, $1 \leqslant q \leqslant 1.4$ describes the amount of off-diagonal latent hardening, i.e. q is the ratio of non-coplanar hardening to coplanar hardening. The isotropic hardening part in Eq. (14) was extended to a saturation-type response in [35]:

$$h = h_0 \operatorname{sech}^2\left|\frac{h_0\gamma}{\tau_s - \tau_0}\right|, \tag{15}$$

where h_0 is the initial hardening modulus, τ_0 is the yield stress which equals the initial value of current strength $\tau_r^\alpha(\gamma = 0)$, τ_s is the (saturated) stage I stress, where rapid hardening commences, and γ is the Taylor cumulative shear strain on all slip systems, i.e.:

$$\gamma = \sum_{\alpha=1}^{N} \int_0^t |\dot\gamma^\alpha|\,\mathrm{d}t. \tag{16}$$

The hardening law in Eq. (15) does not account for rapid hardening (stage II) and parabolic hardening (stage III) in the work-hardening characteristics for fcc single crystals. In the present work, however, it is sufficient to fit the

crystal plasticity hardening model to the experimental stress–strain curve of the considered single crystal.

2.3. Aspects of mechanical modeling of CMSX-4 at room temperature

2.3.1. Material composition

The material in the indentation test is CMSX-4, a two-phase Ni-base superalloy, where semicoherent, ordered Ni_3Al precipitates of $L1_2$ type (γ'-phase) are embedded in a Ni-matrix of fcc structure (γ-phase). The volume fraction of the precipitates is approximately 70%. On account of its considerable creep resistance at high temperatures, the single-crystalline alloy is used for turbine blades in aircraft turbines and in industrial gas turbines for power generation (for a comprehensive overview, see e.g. [36]).

The pyramidal indent diameter of $\bar{d} \approx 60$ μm–as a characteristic length of the present mechanical setting–is well above the size of a single precipitate, $d_p \approx 0.4$–0.5 μm, as the characteristic microstructural length. Two conclusions can be drawn. (1) The material is expected to exhibit a homogenized response concerning the overall deformation behavior, where the two-phase composition can be neglected in modeling. (2) The applied load level during indentation (max $F = 4.905$ N) along with the indent diameters (>50 μm) suggest that ISEs play a subordinate role [15]. Consequently, modeling the plastic behavior of CMSX-4 in the present investigation does not require the incorporation of a constitutive internal length by means of, for example, plastic strain gradients or the density of geometrically necessary dislocations.

2.3.2. Elastoplastic material parameters

Table 1 lists the material data for CMSX-4 at room temperature. The elastic constants c_{11}, c_{12} and c_{44} are taken from [37]. The Young's moduli in Table 1 quantify the orientation dependence of elastic stiffness of the alloy. Effective elastic moduli are maximum in the $\langle 1\,1\,1\rangle$ directions and minimal in the $\langle 0\,0\,1\rangle$ directions. The Zener anisotropy measure $AR = 2c_{44}/(c_{11} - c_{12})$ for CMSX-4 equals 2.85 (isotropy $AR = 1$), thus indicating an elastic anisotropy of intermediate strength compared with other fcc crystals (Pb: 4.14, Cu: 3.21, Au: 2.85, Ni: 2.51, Al: 1.22, data taken from [38]). Elementary mechanical reasoning tells us that stress is attracted by stiffness, i.e. that directions of high elastic stiffness attract the load. Imagine the case of a roughly uniform strain distribution. Plastic yielding will then start first in the stiff $\langle 1\,1\,1\rangle$ directions, next in the $\langle 1\,1\,0\rangle$ directions, and finally in the $\langle 1\,0\,0\rangle$ directions. This aspect will come into play during the subsequent analysis, where the driving mechanism that governs anisotropic pile-up formation during indentation will be identified.

Table 1
Material data of CMSX-4 at room temperature.

Parameter	Symbol	Value	Unit
Elastic moduli	c_{11}	252	GPa
	c_{12}	161	GPa
	c_{44}	131	GPa
Young's moduli in $[ijk]$ direction	$E_{[111]}$	347	GPa
	$E_{[110]}$	253	GPa
	$E_{[100]}$	139	GPa
Reference strain rate	$\dot{\gamma}_0^\alpha$	0.001	1/s
Initial slip resistance	τ_0	260	MPa
Saturation slip resistance	τ_s	775	MPa
Power law exponent	m	20	1
Initial hardening modulus	h_0	350	MPa
Hardening ratio	q	1.4	1

The hardening behaviors in different crystallographic directions generally differ from one another (e.g. [39]). Ref. [40] has reported for a Ni-base single-crystalline superalloy in tension that the hardening rate in the $\langle 1\,1\,1\rangle$ directions is much larger than in the $\langle 1\,0\,0\rangle$ directions and that in the $\langle 1\,1\,0\rangle$ directions there is virtually no hardening capacity.

In the present analysis the data for plastic yielding in Table 1 are chosen to fit the stress–strain curve as reported in Ref. [12] (see Fig. 1). In that reference, compression tests of [001] oriented cylindrical samples were performed at room temperature. Here, parameter $m = 0.02$ in Eq. (8) is chosen at a small value to ensure material behavior close to rate-independence.

3. Indentation experiment and surface reconstruction

In Ref. [41], a Vickers-indenter made of diamond was pressed into an $(0\,0\,1)$ oriented CMSX-4 specimen with a maximum applied load of 4.905 N (500 g). The angle between the pyramid's opposite faces was 136°. Azimuthal orientations ϕ between the indenter's diagonal and the $\langle 0\,0\,1\rangle$ direction were systematically varied in order to obtain Vickers hardness as a function of this orientation.

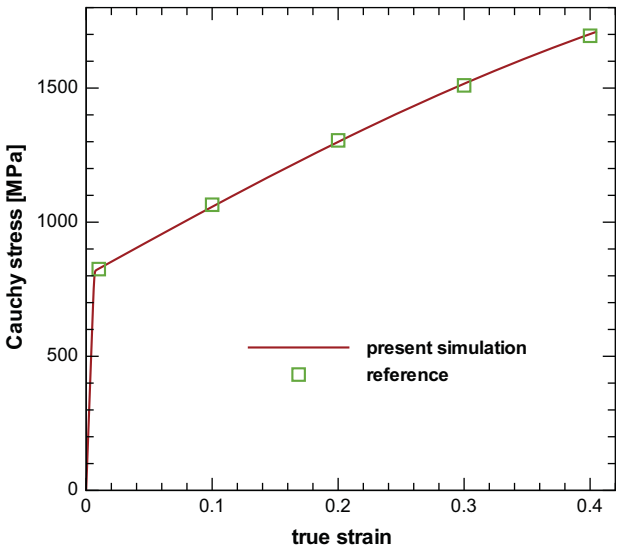

Fig. 1. Stress–strain curve for a compression test of [001] oriented cylindrical samples at room temperature. The reference data follow from experiments reported in Ref. [12].

Force–displacement curves, however, were not recorded in these indentation experiments.

The material sample of Ref. [41] is used in the present work to experimentally obtain 3-D data of the pile-up distribution and shape of the pyramidal indents by SEM (commercial JEOL and Hitachi S520a microscopes). The reconstruction of a digital elevation model (DEM) of the indentation craters from electron backscatter diffraction (EBSD) images (commercial version of Point Electronic) was realized by advanced algorithms in an image-processing software system (commercial version of Alicona).

It is worth pointing out a particular difficulty in data acquisition for surface reconstruction and its solution in the present work. If conventional stereographic images are employed, the successful surface reconstruction in a digital elevation model critically depends on sufficient optical heterogeneity (points, lines, etc.) of the specimen's surface. Since the third dimension is recovered by a comparison of identical material points in different stereo images, the reconstruction fails for two types of objects: (i) if the surface does not provide enough texture on the surface and (ii) if the surface has a recurrent structure.

Here, the indented specimen of CMSX-4 was polished prior to indentation. As a consequence, the surface did not provide sufficient heterogeneity as landmarks for the image-processing software. This applied both for stereo images from light-microscopy as well as for conventional SEM. In the present work the problem was solved by feeding the image-processing software with images obtained from the simultaneous acquisition of four single frames generated by separate signals from a backscatter electron detector.

4. Finite-element simulations

In the finite-element simulations we consider three distinct cases for the azimuthal orientation of the pyramidal indenter, $\phi = 0°$, 22.5°, 45°, where ϕ is the angle between the indenter's diagonal and the $\langle 0\,0\,1\rangle$ direction (cf. Fig. 2).

In order to check whether the finite-element solutions preserve the material symmetry during elastoplastic deformations, the simulations for azimuthal orientations $\phi = 0°$ and $\phi = 45°$ are performed for a quarter system, thus exploiting only two of the total of four symmetry planes (see Fig. 2). For orientation $\phi = 22.5°$ the symmetries of the indenter do not coincide with the material's symmetries, such that full discretization of the indented half-space must be considered in this case.

Finite-element simulations are conducted by means of an 8-node brick-type element (*C3D8*) in the commercial software system [27]. The indented half-space is modeled as a cylinder of radius $r = 660\,\mu m$ and thickness $t = 630\,\mu m$. The non-uniform discretization a priori reflects the region of indentation exhibiting large gradients in plastic deformations (see Fig. 3).

The chosen finite-element meshes are well-suited to describe the surface deformation patterns with high resolution and avoid locking effects, i.e. artificial stiffening effects. Low-order displacement-type finite elements generally exhibit undesired effects such as these for coarse discretizations and for incompressible material laws (volume locking). In the present study, tests on different discretizations have ensured that the final results obtained on fine meshes as in Fig. 3 do not suffer from locking and are close to the converged solution.

The computational box is supported in the z-direction at the bottom and is free at the cylindrical outer face. In the implicit finite-element simulations a unilateral contact formulation with the penalty-method is applied. The Vickers-indenter made of diamond is modeled to be rigid, the influence of friction is neglected.

5. Simulation versus experiment

5.1. Pile-up pattern and indent shape

The experimental results reveal the formation of four distinct pile-up hillocks, each in the $\langle 1\,1\,0\rangle$ directions, which reflects the material's 4-fold symmetry of the fcc crystal in the plane of indentation. The distribution of material pile-up remains hidden in the 2-D view of the experiment (see Fig. 4, left column), but becomes apparent via the contour lines of the simulation results (Fig. 4, right column).

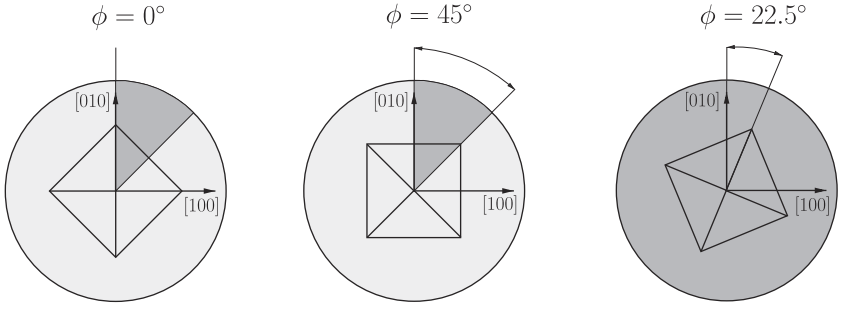

Fig. 2. Azimuthal orientations of the indenter in the simulations, for $\phi = 0°$, $\phi = 45°$ and $\phi = 22.5°$. The shaded sector is the minimal region for finite-element analysis exploiting all existing symmetries.

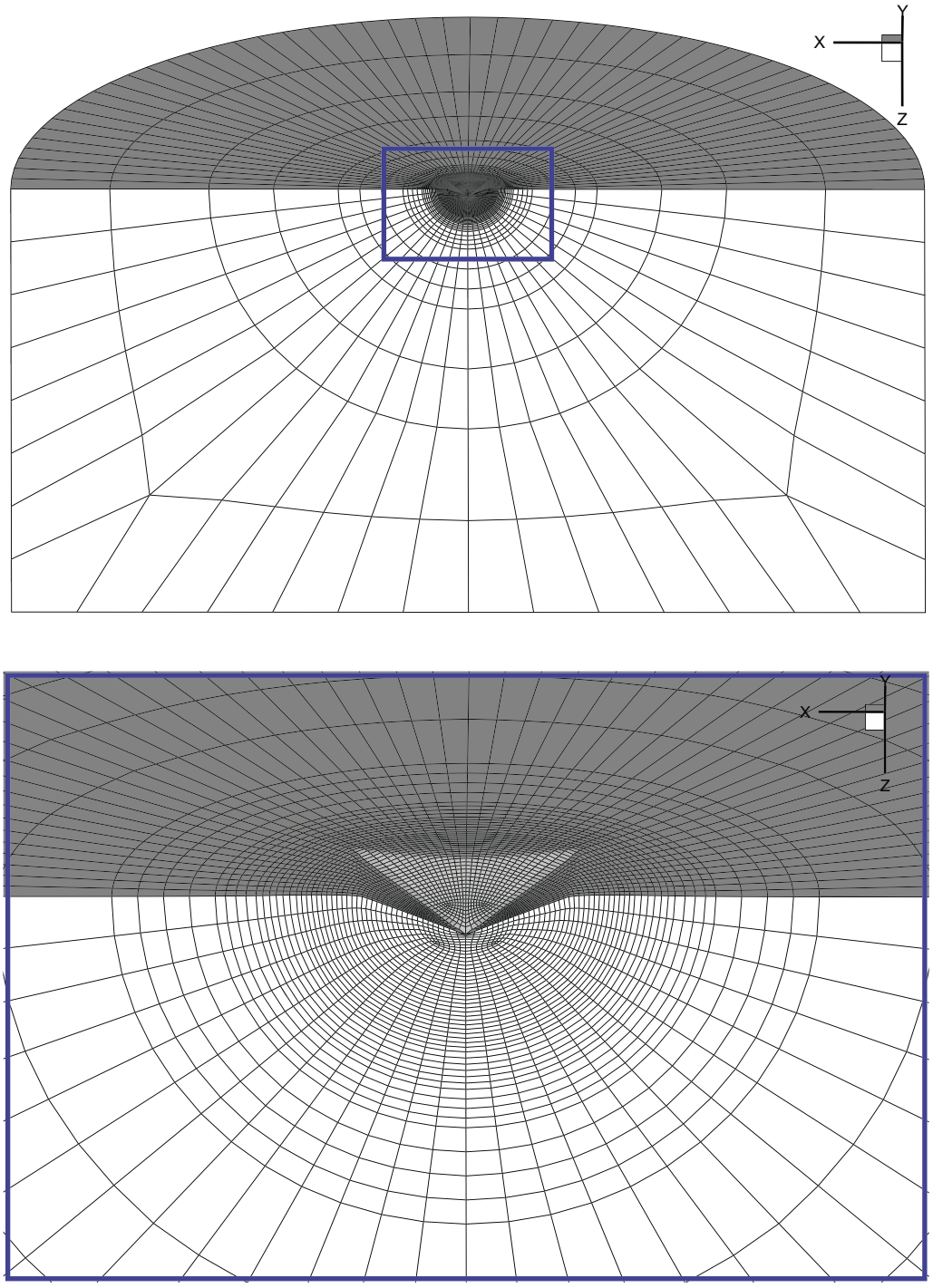

Fig. 3. Cross-sectional view of the finite-element mesh for indentation simulations. The zoomed area in the frame shows the deformed mesh around the indentation crater upon release of the load for orientation $\phi = 45°$.

The simulations predict maximum pile-up in the $\langle 1\,1\,0 \rangle$ directions for $\phi = 0°$, 22.5°, 45° thus being independent of the azimuthal orientation of the pyramidal indenter. Note that the contour lines are cut-off in the interior of the indents. Table 2 reports the maximum values of pile-up and the maximum indentation depth for the applied load.

Pile-up increases the contact area at the indenter's faces; for $\phi = 0°$, the contact area is locally extended in $\langle 1\,1\,0 \rangle$ directions leading to a convex contact rim or a *barrel*-shape (Fig. 4, first row). For $\phi = 45°$, when the pyramid's diagonals align with $\langle 1\,1\,0 \rangle$ directions such that pile-up is maximum at the corners, a concave shape or *pin-cushion* shape of the indent is observed (Fig. 4, third row). For

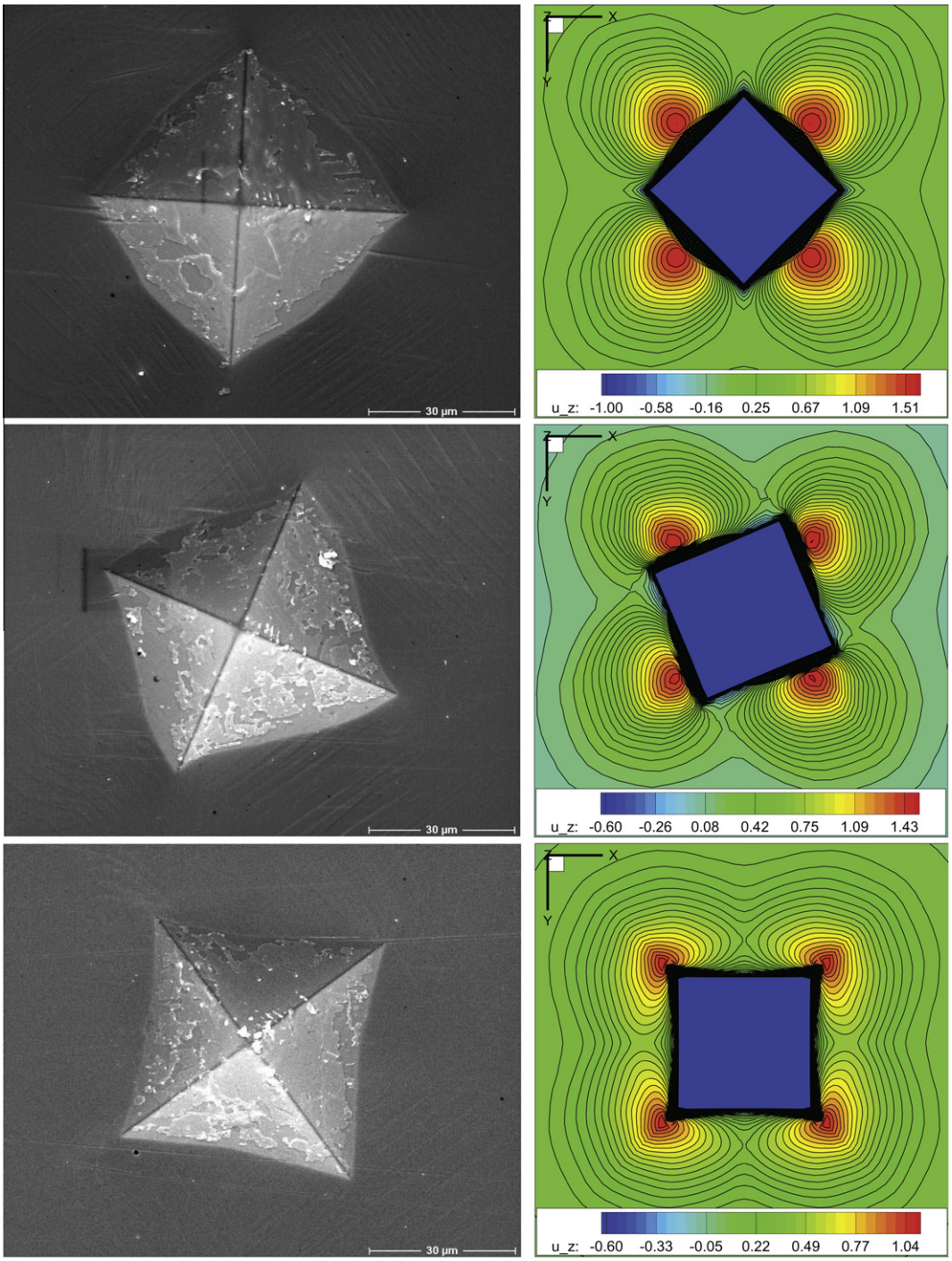

Fig. 4. Pyramidal indentation experiments into (001) fcc CMSX-4. Left: experiment (SEM); right: simulation with isolines of height, u_z (µm), for azimuthal orientation angle $\phi = 0°$, 22.5°, 45° in row 1–3. In the coordinate system, *X*-, *Y*-, *Z*-axes each represent ⟨001⟩ directions. The white stains in the experimental indentation craters is debris from sputtering.

Table 2
Geodesy of the indentation crater in terms of maximum pile-up, max u_z and indentation depth, min u_z for different azimuthal orientations ϕ.

Azimuthal orientation	$\phi = 0°$	$\phi = 22.5°$	$\phi = 45°$
max u_z (µm)	1.59	1.51	1.10
min u_z (µm)	−10.15	−8.95	−9.77

the azimuthal orientations, $\phi = 0°$ and 45°, the symmetries of the indenter coincide with the symmetries of the crystal in the indented (001) plane. For the azimuthal orientation of $\phi = 22.5°$, however, each edge of the contact zone exhibits a change in curvature, from convex in the ⟨110⟩ directions to concave. In conclusion, the curvature of the contact rim reflects the local adaption of the emerging pile-up to the indenter faces.

The different indent shapes in the crystal plasticity simulation agree well with the experiments. The high density of contour lines at the indent's rim in Fig. 4, right column,

highlights the locally extended contact zones. Summarizing, simulation and experiment are in qualitative agreement with respect to the crystallographic pile-up topography, which is constantly maximum in the ⟨1 1 0⟩ directions, and with respect to the local adaption of pile-up to the indenter faces, leading to a corresponding curvature of the contact boundaries each. No matter what the azimuthal orientation of the indenter may be, pile-up is mainly dependent on the sample's crystallographic orientation, i.e. pile-up forms in the ⟨1 1 0⟩ directions.

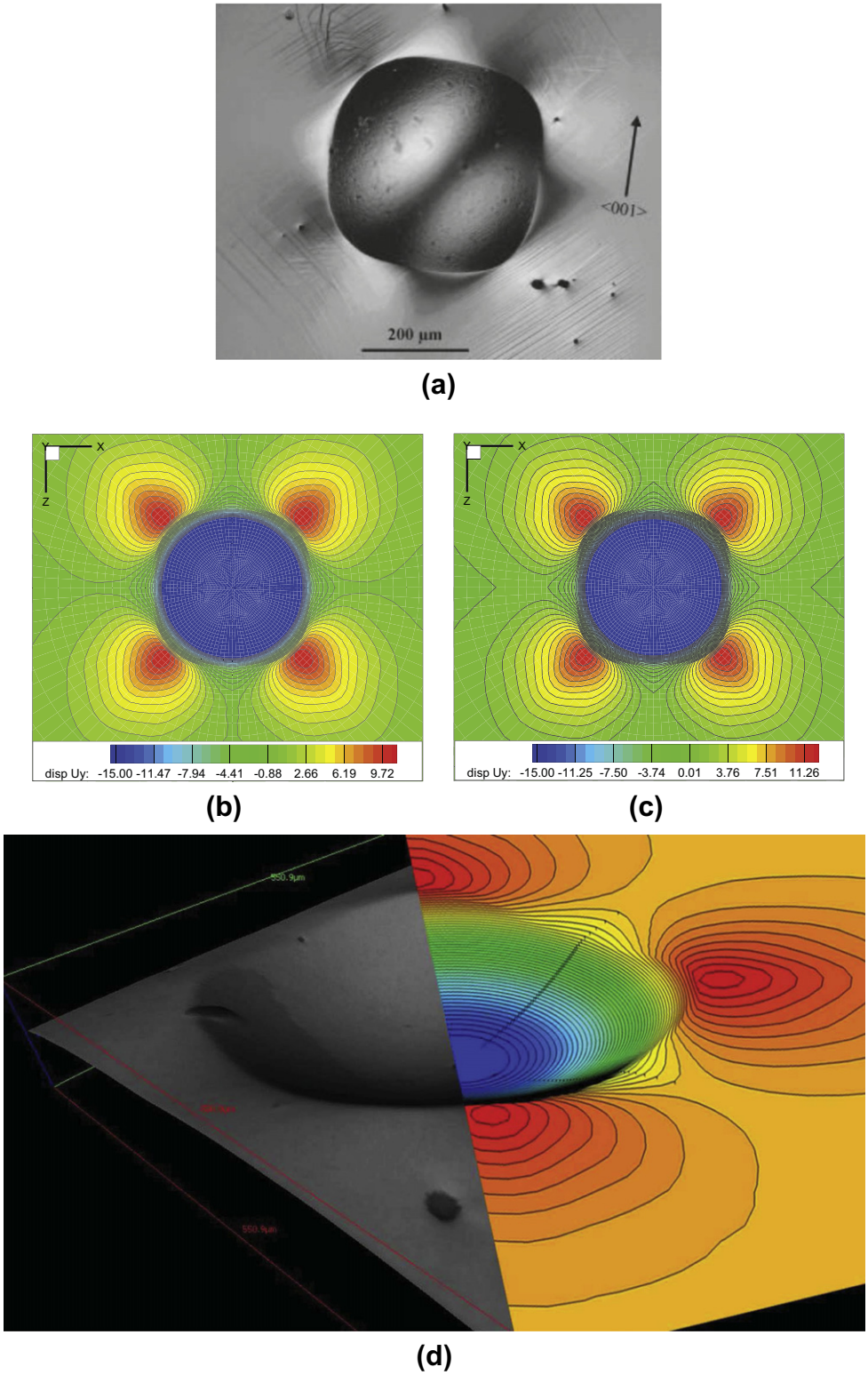

Fig. 5. Spherical indentation into (0 0 1) fcc single crystal: (a) micrograph from experiment [41], simulations with isolines of height, u_y (µm), for (b) cubic elasticity versus (c) isotropic elasticity, (d) perspective view on the indent in experiment (left) and simulation (right).

6. Discussion: is the driving mechanism purely crystallographic?

6.1. The role of indenter orientation

The fact that the pile-up distribution does not critically depend on the azimuthal orientation of the indenter supports the idea that pile-up formation is determined by crystallographic processes rather than by the stress distribution pattern, induced under the non-isotropic pyramidal indenter.

6.2. The role of indenter shape

This conclusion is even fostered by a comparison with the results of spherical indentation into (0 0 1) oriented CMSX-4 in experiment and simulation (see Fig. 5), where the indenter radius is $R = 1.25$ mm, force $F = 490.25$ N and the X-, Y-, Z-axes each align with $\langle 0\,0\,1\rangle$ directions.

The observed pile-up hillocks emerging equally in the $\langle 1\,1\,0\rangle$ directions prove the invariance of the driving process with respect to stress distributions induced by different indenter geometries and orientations.

As a consequence, the driving process for pyramidal indentation can be illustrated similarly for spherical indentation (see Fig. 6 and its caption).

6.3. The role of elastic anisotropy

The relative invariance of pile-up with respect to (i) the azimuthal orientation of the pyramidal indenter and (ii) the geometrical shape of the indenter (pyramidal or spherical) does not strictly prove that pile-up is purely crystallographic, i.e. merely dependent on the specific geometry and orientation of discrete slip systems. The influence of the anisotropy in the elasticity law on the overall elasto-plastic material response is not yet clear. As already pointed out in Section 2.3.2, directions of large elastic stiffness attract stress. Hence, in view of the elastic anisotropy in terms of the Young's moduli $E[ijk]$ in Table 1, plastic yielding is expected to commence first in the stiff $\langle 1\,1\,1\rangle$ directions, next in the $\langle 1\,1\,0\rangle$ directions, and last in the $\langle 1\,0\,0\rangle$ directions; this order may influence the observed pile-up formation, which is strongest in the $\langle 1\,1\,0\rangle$ directions.

In order to quantify the influence of elastic anisotropy on pile-up, we single out its influence by combining isotropy in the elastic law ($AR = 1$) while maintaining the anisotropy of plastic flow. Elastic constants of this fictitious comparison solid are chosen such that the isotropic Young's modulus equals that of CMSX-4 in the $\langle 1\,1\,1\rangle$ direction, $E := E[1\,1\,1] = 347$ GPa; Poisson's ratio is set to $\nu = 0.3$.

The result of the isotropic simulation yields a final surface deformation pattern which is even quantitatively very close to the one applying anisotropic elasticity (cf. Fig. 5b and c). Data to substantiate this fact; for isotropic elasticity we obtain: max $u_z = +12.2$ μm, min $u_z = -50.5$ μm; for cubic elasticity: max $u_z = +10.6$ μm, min $u_z = -52.9$ μm.

In conclusion, pile-up is purely of crystallographic nature, and the direction-dependent stress distribution governed by elastic anisotropy is also negligible.

6.4. Similar phenomena due to different driving mechanisms

Indents of a convex barrel-shape and pin-cushion-shape as in the present analysis of fcc single crystals are well-known phenomena of a different class of material, namely

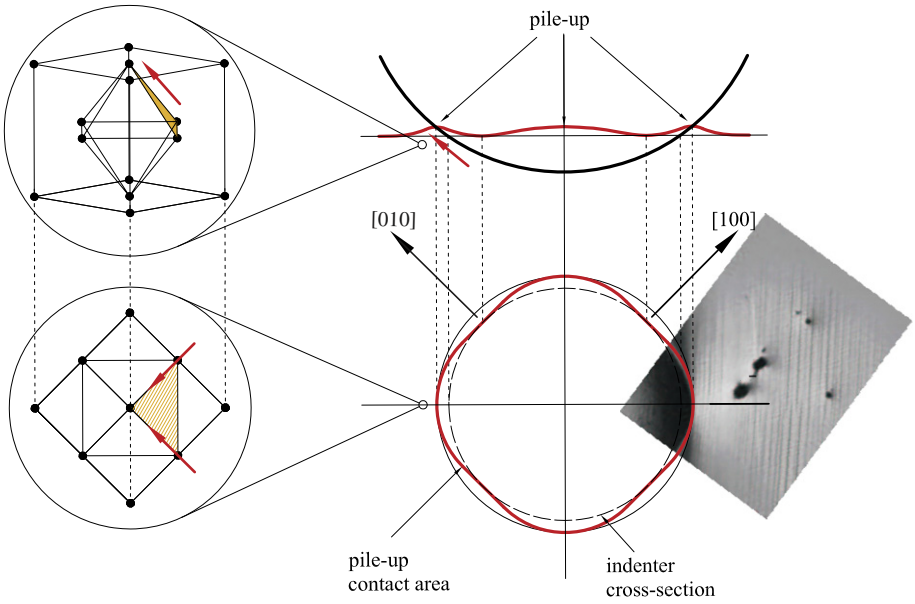

Fig. 6. Pile-up pattern and discrete slip traces at the surface indicate that the driving mechanism for pile-up in the $\langle 1\,1\,0\rangle$ directions is plastic slip in octahedral $\{1\,1\,1\}$ glide planes with the $\langle 1\,1\,0\rangle$ slip directions. One of these glide planes is highlighted; arrows in activated slip systems indicate the direction of material transport up to the surface.

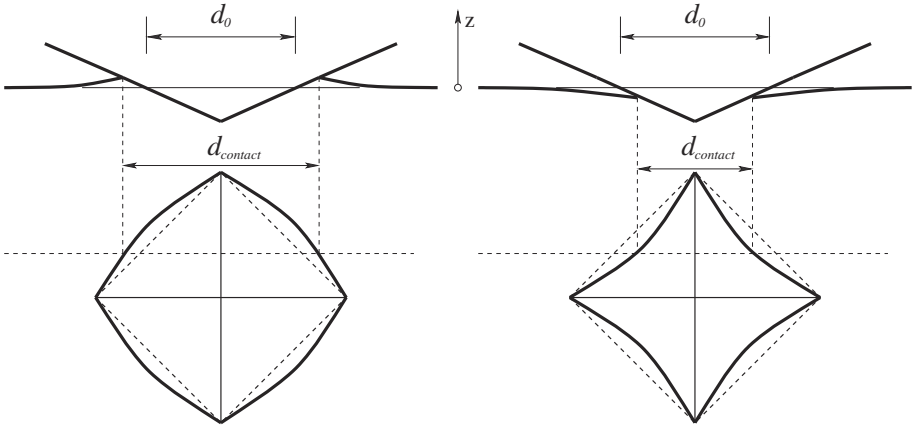

Fig. 7. Pyramidal indentation into quasi-isotropic polycrystals exhibits (left) for a low strain-hardening rate a convex shape due to material pile-up along with locally extended contact zones ($d_{contact} > d_{z=0}$); and (right) for a high strain-hardening rate a concave shape due to sink-in along with locally reduced contact zones ($d_{contact} < d_{z=0}$).

quasi-isotropic polycrystals [42–44]. Although–from bird's eye view–the indents in both materials look similar, compare Fig. 7 with Fig. 4 (first row and third row), the corresponding surface topography and the underlying driving mechanism are completely different.

Quasi-isotropic polycrystals in general exhibit pile-up for a small hardening rate, which leads to a convex bulge-out (barrel-shape) in case of pyramidal indentation (Fig. 7, left). A high strain-hardening rate, in contrast, generally exhibits sink-in, leading to a concave bow-in (pin-cushion-shape) of the decreased contact surface (Fig. 7, right). Put differently, the driving mechanism which shapes the indents of quasi-isotropic polycrystals is the cumulative response of a large number of interacting dislocations thus living on a mesoscopic length scale.

For fcc single crystals, in contrast, it is the discrete nature of plastic slip in certain glide systems existing on the length scale of atomic spacing. As such, the latter mechanism is invariant across the scales and the 4-fold symmetry in pile-up of (0 0 1) fcc single crystals is equally observed on quite different length scales; in the present work for indent diameters of 400 μm, of 1 μm in [6], and of 0.1 μm in [45].

The overlap of both driving mechanisms, the work-hardening rate with the crystallographic plastic flow, has been analyzed in Ref. [11] for (0 0 1) fcc single-crystalline material subject to spherical indentation. The finite-element simulations predict that it is, in the first place, a considerable increase in the rate of work-hardening, that shapes the anisotropy of the surface pattern in terms of direction-dependent pile-up and sink-in.

7. Conclusions

The present contribution has analyzed pyramidal indentation into (0 0 1) fcc single crystal in experiment and in crystal plasticity finite-element simulations. The main findings and conclusions can be summarized as follows:

(i) The indents reflect the material's cubic symmetry in that for different azimuthal orientations of the pyramid, pile-up patterns invariantly emerge in the ⟨1 1 0⟩ directions. If a pyramid's diagonal is aligned with a ⟨1 1 0⟩ direction, the contact zone at the indenter faces is concave. If a diagonal is aligned with a ⟨1 0 0⟩ direction, the contact zone at the indenter faces exhibits a convex bulge-out. In between these orientations a contact rim of mixed, convex–concave curvature is induced. Thus, the geometrically non-isotropic pyramidal indenter locally breaks the cubic symmetry of the crystal for azimuthal orientations of the diagonal, which are different from ⟨1 0 0⟩ and ⟨1 1 0⟩. Notwithstanding, apart from these local effects, where the adaption of the indenter's geometry to the pile-up hillocks leads to different indent shapes, pile-up pattern invariantly emerge in ⟨1 1 0⟩ directions.

(ii) Observations (i), seen in experiment and simulation, along with the slip traces at the indented surfaces, indicate that pile-up is induced by glide on {1 1 1} ⟨1 1 0⟩ slip systems. It is mainly the geometry of the slip systems in the (0 0 1) oriented crystal which govern pile-up, whereas stress concentrations introduced by different indenter shapes, by the azimuthal orientation of a pyramidal indenter and also by the characteristics of the elasticity law, have no significant influence.

(iii) Although phenomenologically very similar in kind, the driving mechanism behind the curved indent shapes are completely different from those in quasi-isotropic polycrystals. In the fcc single crystal case, the process is primarily driven by crystallographic slip on specific slip-planes. For quasi-isotropic polycrystals, in contrast, it is a high strain-hardening rate of the material inducing sink-in accompanied by a pin-cushion indent shape and a low strain-hardening rate inducing pile-up accompanied by a barrel indent shape.

(iv) The crystal plasticity model accounting for glide in octahedral $\{111\}\ \langle 110\rangle$ slip systems for fcc crystalline material predicts in finite-element simulations the pile-up pattern formation and the material's local accomodation to the indenter.

Acknowledgements

The author is grateful to Klaus Wintrich for providing the CMSX-4 specimen for the present measurements using SEM and EBSD and to Marco Schürg for assistance in preparing optimized FE meshes. The author acknowledges financial support through ThyssenKrupp AG, Bayer MaterialScience AG, Salzgitter Mannesmann Forschung GmbH, Robert Bosch GmbH, Benteler Stahl/Rohr GmbH, Bayer Technology Services GmbH and the state of North-Rhine Westphalia as well as the European Commission in the framework of the European Regional Development Fund (ERDF).

References

[1] Dyer LD. Trans ASM 1965;58:620.
[2] Chang SC, Chen HC. Acta Metall Mater 1995;43:2501.
[3] Stelmashenko NA, Brown LM. Philos Mag A 1996;74:1195.
[4] Nibur KA, Bahr DF. Scripta Mater 2003;49:1055.
[5] Hollatz M, Bobeth M, Pompe W, Marx V. Acta Mater 1996;44:4149.
[6] Wang Y, Raabe D, Klüber D, Roters F. Acta Mater 2004;52:229.
[7] Zaafarani N, Raabe D, Singh RN, Roters F, Zaefferer S. Acta Mater 2006;54:1863.
[8] Zaafarani N, Raabe D, Roters F, Zaefferer S. Acta Mater 2008;56:31.
[9] Liu Y, Wang B, Yoshino M, Roy S, Lu H, Komanduri R. J Mech Phys Solids 2005;53:2718.
[10] Liu Y, Varghese S, Ma J, Yoshino M, Lu H, Komanduri R. Int J Plast 2008;24:1990.
[11] Eidel B, Gruttmann F. Comput Mater Sci 2007;39:172.
[12] Zambaldi C, Roters F, Raabe D, Glatzel U. Mater Sci Eng A 2007;454–455:433.
[13] Casals O, Forest S. Comput Mater Sci 2009;45:774.
[14] Zambaldi C, Raabe D. Acta Mater 2010;58:3516.
[15] Stelmashenko NA, Walls MG, Brown LM, Milman YV. Acta Metall Mater 1993;41:2855.
[16] Kovács Zs, Chinh NQ, Lendvai J. J Mater Res 2001;16:1171.
[17] Peralta P, Ledoux R, Dickerson R, Hakik M, Dickerson P. Metall Mater Trans A 2004;35:2247.
[18] Casals O, Očenášek J, Alcalá J. Acta Mater 2007;55:68.
[19] Alcalá J, Casals O, Očenášek J. J Mech Phys Solids 2008;56:3277.
[20] Taylor GI. J Inst Metals 1938;62:307.
[21] Hill R. J Mech Phys Solids 1965;13:89.
[22] Theodosiu C. In: Simmons JA, editor, Proceedings of the conference on fundamental aspects of dislocation theory, US National Bureau of Standards; 1970. p. 837.
[23] Rice J. J Mech Phys Solids 1971;19:433.
[24] Hill R, Rice J. J Mech Phys Solids 1972;20:401.
[25] Asaro RJ. J Appl Mech 1983;50:921.
[26] Asaro RJ, Needleman A. Acta Metall 1985;33:923.
[27] ABAQUS/Standard, 2009. Theory and user's manual, Version 6.9, ABAQUS Inc.
[28] Huang Y. Mech. report 178, Cambridge (MA): Division of Applied Sciences, Harvard University; 1991.
[29] Kysar JW. Addendum to 'A user-material subroutine incorporating single crystal plasticity in the ABAQUS finite element program'. Mech. report 178, Cambridge (MA): Division of Applied Sciences, Harvard University; 1997.
[30] Asaro RJ, Rice JR. J Mech Phys Solids 1977;25:309.
[31] Kröner E. Arch Ration Mech Anal 1960;4:273.
[32] Lee EH. J Appl Mech 1969;36:1.
[33] van der Giessen E, Besseling JF. Mathematical modelling of inelastic deformation. London: Chapman & Hall; 1994.
[34] Hutchinson JW. Proc Roy Soc A 1970;319:247.
[35] Pierce D, Asaro RJ, Needleman A. Acta Metall 1983;31:1951.
[36] Reed RC. The superalloys: fundamentals and applications. Cambridge: Cambridge University Press; 2006.
[37] Siebörger D, Knake H, Glatzel U. Mater Sci Eng A 2001;298:26.
[38] Simmonds D, Wang H. Single crystal elastic constants and calculated aggregate properties: a handbook. 2nd ed. Cambridge (MA): MIT Press; 1970.
[39] Kocks UF, Mecking H. Prog Mater Sci 2003;48:171.
[40] Westbrooke EF, Forero LE, Ebrahimi F. Acta Mater 2005;52:2137.
[41] Wintrich K. Schädigungsverhalten der einkristallinen Superlegierung CMSX-4 bei Hochtemperaturbelastung. Ph.D. Dissertation, TU Darmstadt; 2004. (in German)
[42] Bolshakov A, Pharr GM. J Mater Res 1998;13:1049.
[43] Giannakopoulos AE, Suresh S. Scripta Mater 1999;40:1191.
[44] Alcalá J, Barone AC, Anglada M. Acta Mater 2000;48:3451.
[45] Kiely JD, Houston JE. Phys Rev B 1998;77(7):12588.